LETTERS
https://doi.org/10.1038/s41550-020-1049-8

nature astronomy

Uranian satellite formation by evolution of a water vapour disk generated by a giant impact

Shigeru Ida[1]✉, Shoji Ueta[2], Takanori Sasaki[3] and Yuya Ishizawa[3]

The ice-giant planet Uranus probably underwent a giant impact, given that its spin axis is tilted by 98 degrees[1–3]. That its satellite system is equally inclined and prograde suggests that it was formed as a consequence of the impact. However, the disks predicted by the impact simulations[1,3,4] generally have sizes one order smaller and masses two orders larger than those of the observed system at present. Here we show, by means of a theoretical model, that the Uranian satellite formation is regulated by the evolution of the impact-generated disk. Because the vaporization temperature of water ice is low and both Uranus and the impactor are assumed to be ice-dominated, we can conclude that the impact-generated disk has mostly vaporized. We predict that the disk lost a substantial amount of water vapour mass and spread to the levels of the current system until the disk cooled down enough for ice condensation and accretion of icy particles to begin. From the predicted distribution of condensed ices, our *N*-body simulation is able to reproduce the observed mass–orbit configuration of Uranian satellites. This scenario contrasts with the giant-impact model for the Earth's Moon[5], in which about half of the compact, impact-generated, solid or liquid disk is immediately incorporated into the Moon on impact[6].

Uranus has five major satellites in a mass range of 10^{-6}–10^{-4} M_U (Fig. 1), where $M_U \simeq 8.7 \times 10^{25}$ kg is the mass of Uranus, extended to about $25r_U$, where $r_U \simeq 2.5 \times 10^7$ m is the physical radius of Uranus (Fig. 1). The extension to about $25r_U$ cannot be accounted for by tidal orbital expansions[7]. Their orbits are prograde to the spin of Uranus and nearly circular. The total mass of the satellites is about $10^{-4}M_U$. The rock-to-ice ratios of the satellites are observationally estimated to be nearly 1:1 except for the innermost satellite, Miranda[8], while Uranus consists mostly of ices[9]. For formation of the satellites, impact[1] and circumplanetary sub-disk[10] scenarios have been proposed. Because the sub-disk that feeds H/He gas from a circumstellar disk to the planet would be formed on the planetary orbital plane, the sub-disk scenario is not compatible with the inclined satellite system, unless multi-step, complicated mechanisms are considered[11]. It is much simpler to consider that the satellites are formed in the disk generated by the impact that tilted the spin axis and caused the current spin period (about 17.2 hours). The accretion of the satellites from the impact-generated disk naturally results in the prograde orbits on the equatorial plane of Uranus. However, the theoretically predicted impact-generated disks[1,3,4] are not only one order smaller and two orders more massive than in the current system but are also substantially depleted in rocky components, because rocks in the small core are not easily ejected by the impact. These difficulties arose in previous work[1,3,4] because the giant-impact model of the Earth's Moon[5] was simply translated to Uranus without taking into account the evolution of the water vapour disk.

We assume that both Uranus and the impactor are ice-dominated with small rocky cores and that Uranus is covered by an atmosphere of 3–10 weight per cent H/He. The Uranus gravity accelerates the impact velocity to $\gtrsim 20\,\mathrm{km\,s^{-1}}$ and, equivalently, the impact energy to $\gtrsim 2 \times 10^8\,\mathrm{J\,kg^{-1}}$, which is 100 times larger than the latent heat of H_2O ice. As a result, the impact-generated disk consists of a mixture of water vapour and H/He gas. Although the icy mantle also includes CH_4 and NH_3 ices, we consider only the most abundant ice, H_2O, as representative of the ices. Since $(c_s/v_K)^2 \simeq 3.3 \times 10^{-2}(\mu_{all}/2.8)^{-1}(T/10^4\ \mathrm{K})(r/r_U) \ll 1$, where T is the disk temperature, c_s is the local velocity of sound, v_K is the local Keplerian velocity, μ_{all} is the mean molecular weight of the mixture, the evaporated vapour does not escape from the Uranian system and remains as a circumplanetary disk.

As we show below, the final satellite mass and orbital distributions are solely determined by a condensation sequence of icy grains in the disk, and the turbulent viscous spreading and cooling of the disk play an essential part in satellite formation. We numerically solve the one-dimensional viscous diffusion equation of disk gas surface density Σ_g, given by[12]:

$$\frac{\partial \Sigma_g}{\partial t} - \frac{1}{r}\frac{\partial}{\partial r}\left[3r^{1/2}\frac{\partial}{\partial r}(\Sigma_g \nu r^{1/2})\right] = 0 \qquad (1)$$

where the turbulent kinetic viscosity is modelled by $\nu = \alpha c_s^2 \Omega^{-1}$, where Ω is the orbital frequency of the disk gas, and α is a constant parameter that represents the turbulence strength ($\alpha \ll 1$)[13]. As local disk temperature, we use the photo-surface temperature by the viscous heating for simplicity[12]:

$$T \simeq \left(\frac{9GM_U\Sigma_g\nu}{8\sigma r^3}\right)^{1/4} \qquad (2)$$

where G is the gravitational constant and σ is the Stefan–Boltzmann constant.

The numerically solved Σ_g and T evolution of the disk is shown in Fig. 2a,b. They show that the impact-generated disk quickly spreads and cools. By the conservation of total angular momentum, the spreading is associated by accretion of the disk onto the planet. The disk converges to a quasi-steady-state accretion disk where the Σ_g and T distributions with radial distance r evolve self-similarly. We derive an approximate expression for the self-similar solution of Σ_g and T in order to generalize the numerical results. For steady accretion (with $\Sigma_g\nu$ constant), $T \propto r^{-3/4}$ (equation (2)) and $\nu \propto c_s^2\Omega^{-1} \propto Tr^{3/2} \propto r^{3/4}$. The self-similar solution to the above equation with time-independent ν has already been derived[12,14]. In our case, ν also depends on Σ_g through T (equation (2)), decreasing with time. We modify the original

[1]ELSI, Tokyo Institute of Technology, Tokyo, Japan. [2]Graduate School of Advanced Integrated Studies in Human Survivability, Kyoto University, Kyoto, Japan. [3]Department of Astronomy, Kyoto University, Kyoto, Japan. ✉e-mail: ida@elsi.jp

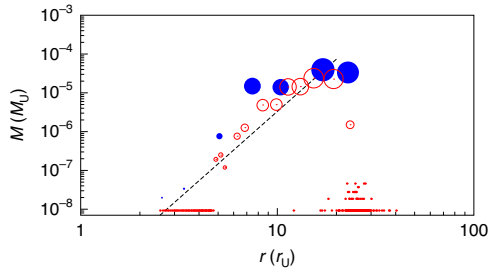

Fig. 1 | The mass (*M*) and orbital radius (*r*) distribution of the current Uranian satellite systems and that predicted by *N*-body simulation. The five major Uranian satellites are represented by the filled blue circles in the range $M \gtrsim 10^{-6}\,M_U$ and $r \gtrsim 5r_U$, where M_U and r_U are the mass and orbital radius of Uranus. Minor satellites with $10^{-8}\,M_U$ to $10^{-7}\,M_U$ are also plotted (tiny filled blue circles). The size of the circles is proportional to the physical radius. The open red circles represent the result of *N*-body simulations of accretion from condensed icy particles (10,000 bodies with masses of $0.92 \times 10^{-8}\,M_U$) at 1,300 years (see Methods). With a longer run, some of the accreted satellites would collide with each other, minor satellites would accrete from the small satellitesimals with $M \simeq 10^{-8}\,M_U$ at $r < 10r_U$ and the satellitesimals with $M \simeq 10^{-7}\,M_U$ at $r > 10r_U$ would be swept by the proto-satellites, which is more consistent with observations of the current Uranian satellites. The dashed black line is the analytically derived 'isolation mass' in the oligarchic growth model of ref. [18] given by equation (11).

self-similar solution incorporating the additional Σ_g-dependence as (Methods):

$$\Sigma_g = \Sigma_{g,U0}\ t_{*0}^{-21/22}\left(\frac{r}{r_U}\right)^{-3/4}\exp\left[-\left(\frac{r}{r_{d0}t_{*0}^{-12/22}}\right)^{5/4}\right] \quad (3)$$

$$t_{*0} = 1 + \frac{t}{t_{diff0}} = 1 + \frac{t}{(16/75)(r^2/\nu)_{r_{d0},t=0}} \quad (4)$$

where $\Sigma_{g,U0}$ is the disk gas surface density at $r = r_U$ and at $t = 0$, t_{diff0} is the viscous diffusion timescale at r_{d0}, and r_{d0} is the characteristic disk radius at $t = 0$, respectively. We define t as the time after the impact-generated disk is relaxed to the quasi-steady-state self-similar solution. The corresponding analytical T is derived from Σ_g with equation (2). The analytical solutions reproduce the numerical results except for the exponential tail (Fig. 2a,b).

The values of r_{d0} and $\Sigma_{g,U0}$ in the analytical solutions are given by the quantities of the impact-generated disk as (see equations (21) and (22) in Methods):

$$r_{d0} \simeq 3.0\left(\frac{\langle r_{d,imp}\rangle}{2\ r_U}\right)\ r_U \quad (5)$$

$$\Sigma_{g,U0} \simeq 6.5\times 10^7\left(\frac{\langle r_{d,imp}\rangle}{2r_U}\right)^{-5/4}\left(\frac{M_{d,imp}}{10^{-2}M_U}\right)\ \mathrm{kg\ m^{-2}} \quad (6)$$

where $M_{d,imp}$ is the total mass of the impact-generated disk, $\langle r_{d,imp}\rangle$ is its mean orbital radius defined by $\langle r_{d,imp}\rangle = \left((J_{d,imp}/M_{d,imp})/r_U^2\Omega_U\right)^2\ r_U$, $J_{d,imp}$ is its total angular momentum, and Ω_U is the disk orbital frequency at $r = r_U$. Thus, we have demonstrated that the disk spreading and cooling are mostly determined by only two parameters, $\langle r_{d,imp}\rangle$ and $M_{d,imp}$, independently of other details of the impact-generated disk. The past-impact simulations[1,3,4] showed that $\langle r_{d,imp}\rangle \simeq 2r_U$ and $M_{d,imp} \simeq 10^{-2}\,M_U$ are typical values.

When the disk temperature decays to the ice condensation temperature $T_{ice} \simeq 240\,\mathrm{K}$ (equation (49) in Methods) for the first time, we deposit the condensed ice surface density by $\Sigma_{ice} = \gamma\Sigma_g$, where γ is the abundance of water vapour in the disk. Smooth particle hydrodynamics (SPH) simulations suggest $\gamma \simeq 0.1 - 0.5$ (refs. [1,3,4]). We use $\gamma = 0.3$ as a nominal value and $\gamma_{03} = \gamma/0.3$. With $T \simeq 240\,\mathrm{K}$, the numerically obtained Σ_{ice} and deposited radius ('ice line') r_{ice} are plotted in Fig. 2c,d. Because ice condensation occurs after substantial evolution of the quasi-steady-state disk, the ice distribution is independent of the detailed structure of the initial impact-generated disk. In particular, Σ_{ice} at each r is independent of $M_{d,imp}$ (Fig. 2c), and the analytical estimation of Σ_{ice} below shows that it is independent even of $\langle r_{d,imp}\rangle$. From equation (2):

$$T \simeq 240\left(\frac{\alpha}{10^{-3}}\right)^{1/3}\left(\frac{\Sigma_g}{4.0\times 10^2\,\mathrm{kg\,m^{-2}}}\right)^{1/3}\left(\frac{r}{r_U}\right)^{-1/2}\ (\mathrm{K}) \quad (7)$$

From equation (7) with $T_{ice} \simeq 240\,\mathrm{K}$, we obtain:

$$\Sigma_{ice} \simeq \gamma\Sigma_g \simeq 1.2\times 10^2\beta^{-1}\gamma_{03}\left(\frac{r}{r_U}\right)^{3/2}\ \mathrm{kg\ m^{-2}} \quad (8)$$

where $\beta = (\alpha/10^{-3})(T_{ice}/240\,\mathrm{K})^{-3}$. This completely reproduces Σ_{ice} by the numerical solution (Fig. 2c).

The positive gradient of Σ_{ice} ($\propto r^{3/2}$) is produced from Σ_g with the negative slope ($\propto r^{-3/4}$), because, in inner regions, the viscous heating is more efficient (equation (2)) and the disk must be more significantly depleted to realize $T \lesssim T_{ice}$ than in outer regions. The positive gradient implies that most of the condensed ice mass is located in an outermost region. Although Σ_{ice} does not depend on $\langle r_{d,imp}\rangle$ and $M_{d,imp}$ at each r, they affect how far the distribution extends, although the dependencies are weak. The outer truncation radius for the Σ_{ice}-distribution is evaluated as below; it reproduces the numerical results.

The ice condensation occurs when the gas temperature T exceeds T_{ice} for the first time at individual r. As the gas disk further expands, T in the outer regions becomes well below T_{ice}. However, icy grains do not condense there, because the ices have already condensed and the gas there is free of water vapour. The maximum radius r_{max} of the ice condensation is estimated by the intersection of equation (8) and the envelope curve of the superposition of the Σ_g–r curves at different times (Fig. 2a). It is given by (see Methods and equation (23)):

$$r_{max} \simeq 20\left[\beta\left(\frac{\langle r_{d,imp}\rangle}{2r_U}\right)^{-5/4}\left(\frac{M_{d,imp}}{10^{-2}M_U}\right)\right]^{1/4} r_U \quad (9)$$

From equations (8) and (9), the total condensed ice mass is:

$$M_{ice} \simeq \int_{r_U}^{r_{max}} 2\pi r\Sigma_{ice}\mathrm{d}r \simeq 0.58\times 10^{-4} \times\ \beta^{1/8}\gamma_{03}\left(\frac{\langle r_{d,imp}\rangle}{2r_U}\right)^{-5/4}\left(\frac{M_{d,imp}}{10^{-2}M_U}\right)^{7/8} M_U \quad (10)$$

which is consistent with the current total mass of Uranian satellites (about $1.0 \times 10^{-4}M_U$). Although the turbulent viscosity parameter α is uncertain, the α-dependence of M_{ice} and r_{max} are very weak ($\alpha \propto \beta$). Thus, we have demonstrated that the compact ($\langle r_{d,imp}\rangle \simeq 2r_U$) and massive ($M_{d,imp} \simeq 10^{-2}M_U$) initial disk produces the condensed ice confined at a distant place, $r_{max} \simeq 20\ r_U$ with the highly reduced total mass (about $10^{-4}M_U$). This result clearly solves the problem of a too massive and too compact impact-generated disk.

Once (sub-micrometre) icy grains condense in the disk, they coagulate with one another. In general, as the icy particles grow, the particles drift inward, pulled by the aerodynamic gas drag[15]. However, the disk gas density is depleted so severely before the ice condensation that the growth is much faster than the drift (see Methods) and kilometre-sized 'satellitesimals' are formed in situ

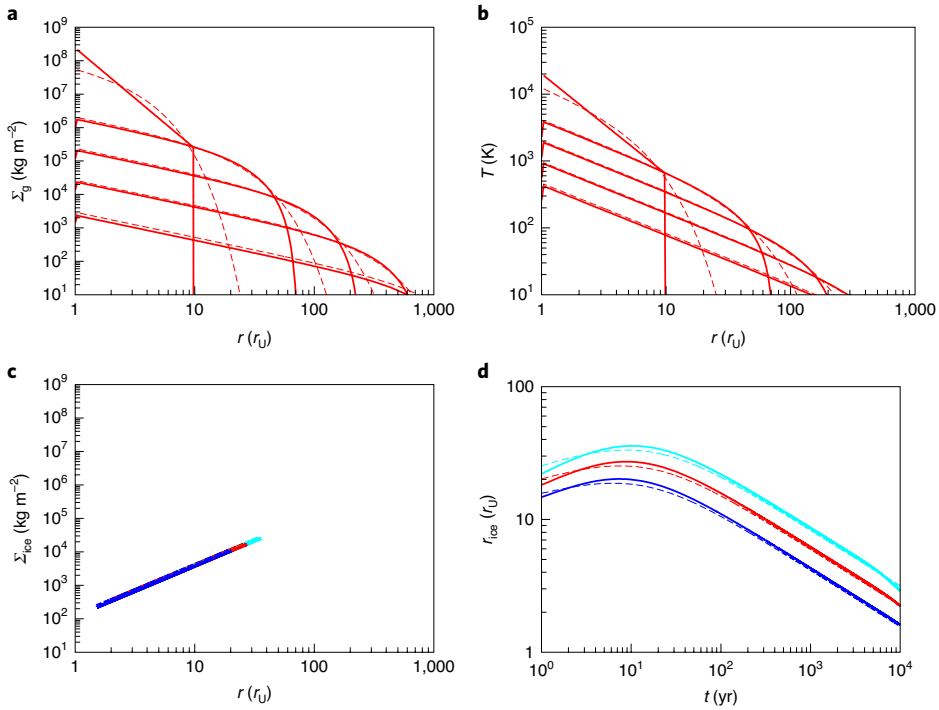

Fig. 2 | The evolution of the disk of a mixture of H/He gas and water vapour and the associated ice condensation. a, The evolution of the disk surface density of a mixture of H/He gas and water vapour Σ_g. **b**, The evolution of the disk temperature T with $\alpha = 10^{-3}$. The solid and dashed red lines are the numerically solved distribution and the analytical distribution (equations (2) and (3)). In panels **a** and **b**, the upper to lower curves for $r < 10r_U$ represent the distributions at $t = 0$, 10, 10^2, 10^3 and 10^4 years. The initial disk for the numerical calculation is set to be centrally confined, $\Sigma_{g,imp} = 2.4 \times 10^8 (r/r_U)^{-3}$ kg m^{-2} with a truncation at $r = 10r_U$, which has $M_{d,imp} = 10^{-2} M_U$ and $\langle r_{d,imp} \rangle \simeq 2.3r_U$. In the analytical self-similar formula, $r_{d0} = 3r_U$ and $\Sigma_{d0} = 0.3\,\Sigma_{g,imp}$ are used, according to the conversion given by equations (5) and (6). **c**,**d**, The time evolution of the ice line is plotted in panel **d**. The blue, red and light blue lines are for $M_{d,imp} = 3 \times 10^{-3} M_U$, $10^{-2} M_U$ and $3 \times 10^{-2} M_U$, respectively. When T becomes equal to T_{ice}, we assume that ice condenses with the surface density $\Sigma_{ice} = \gamma \Sigma_g$ at that time (panel **c**), where we assumed $\gamma = 0.3$.

without radial drift. Owing to the disk gas depletion, 'type I migration' of proto-satellites caused by the torque from density waves in the disk would not be important, either (Methods). Therefore, the satellitesimals and satellites must be formed in situ.

The vaporization of rocks occurs at $T > 2{,}000$ K (ref. [16]). Owing to the high vaporization or condensation temperature, silicate (rock components) grains should quickly re-condense, while the disk is still massive and compact. Our model naturally produces an enhanced rock-to-ice ratio of the satellites because the ices condense after a reduction of water vapour by two orders of magnitude, whereas the rocks condense before substantial reduction has occurred. Although the silicates condense only in the inner region, they would also spread uniformly in the disk. Because silicate particles are not sticky at silicate–silicate collisions[17], they do not grow larger than about 100 μm and they radially spread with the turbulent viscous dissipation in the disk, unless the turbulence is very weak (see Methods). After the disk cools down and ice condensation starts, silicate particles can stick to icy particles or ices may condense to the silicate particle surface beyond the ice line one after another, which could potentially account for a relatively uniform rock-to-ice ratio (about $O(1)$) of all the satellites. Thus, our model may also solve the small rock-to-ice ratio produced by previous simulations[1,3,4], although more detailed investigation is needed.

The condensed ice mass distribution peaks strongly at $\sim r_{max}$. This is consistent with the mass–orbit distribution of Uranian satellites (Fig. 1). We have performed a direct three-dimensional N-body simulation from 10,000 bodies with the individual masses $0.92 \times 10^{-8}\,M_U$ that follow the ice distribution given by equation (8) with $r_{max} = 20\ r_U$ and $\beta = \gamma_{03} = 1$ (Methods). We note that pebble accretion is negligible in our system (Methods). The result reproduces the mass–orbit configuration of the current Uranian satellites in Fig. 1. In a longer run, a more consistent result would be obtained (see the legend to Fig. 1). Because orbital migration of satellites is not important, the satellites are not trapped in resonant orbits, and the mass of accreted satellites is consistent with the isolation mass in the oligarchic growth model of ref. [18], given by (see Methods and equation (53)):

$$\frac{m_{iso}}{M_U} \simeq 0.74 \times 10^{-4} \beta^{-3/2} \gamma_{03}^{3/2} \left(\frac{r}{20 r_U} \right)^{21/4} \tag{11}$$

We also performed N-body simulations from ordinary Σ_{ice}-distributions with a negative radial gradient and robustly showed that a positive gradient of Σ_{ice} is required to reproduce the current mass–orbit configuration[19].

We have shown that the current Uranian major satellites are very well reproduced by the derived analytical formulas based on viscous spreading and cooling of the disk generated by an impact that is constrained by the spin period and the tilted spin, independently of the details of the initial disk parameters. Although we have focused on Uranus, the model here provides a general scenario for satellite formation around ice giants with scaling by the mass and the physical radius of a central planet, which is completely different from satellite-formation scenarios around terrestrial planets and gas giants. It could also be applied to the inner region of Neptune's satellite system, where we can neglect the effect of Triton that may have been captured[20]. Observations suggest that many of the super-Earths discovered in exoplanetary systems may consist of abundant water ice, even in close-in (warm) orbits[21]. The model here may also provide insights into possible icy satellites of super-Earths.

Methods

Theory and numerical analysis. *Approximate self-similar solution to viscous diffusion equation.* The analytical self-similar solution to equation (1) is given by[12,14]:

$$\Sigma_{\rm g} \propto t_*^{-\frac{5/2-\zeta}{2-\zeta}} r^{-\zeta} \exp\left[-\left(\frac{r}{r_{\rm d0}}\right)^{2-\zeta} t_*^{-1}\right] \tag{12}$$

where $\zeta = d\ln\nu/d\ln r$ and $t_* = 1 + t/t_{\rm diff}$:

$$t_{\rm diff} = \frac{1}{3(2-\zeta)^2}\left(\frac{r^2}{\nu}\right)_{r_{\rm d0}} \tag{13}$$

where subscript $r_{\rm d0}$ indicates the value at $r_{\rm d0}$. The surface density is $\propto r^{-\zeta}$ for $r \ll r_{\rm d} = r_{\rm d0}\ t_*^{1/(2-\zeta)}$ and it exponentially decays for $r \gtrsim r_{\rm d}$, so that $r_{\rm d}$ is the characteristic disk radius. In the case of our simple viscous heating model (equation (2)), $\nu \sim \alpha c_{\rm s}^2/\Omega \propto T\ r^{3/2} \propto \Sigma_{\rm g}^{1/3}\ r$. In inner-disk regions, the disk accretion is steady and its rate is independent of r, that is, $\Sigma_{\rm g}\nu$ is independent of r. In this case, $\nu \propto r^{3/4}$. With $\zeta = 3/4$, the self-similar solution given by equation (12) is:

$$\Sigma_{\rm g} = \Sigma_{\rm g,U0}\ t_*^{-7/5}\left(\frac{r}{r_{\rm U}}\right)^{-3/4} \exp\left[-\left(\frac{r}{r_{\rm d0}}\right)^{5/4} t_*^{-1}\right] \tag{14}$$

where $r_{\rm U}$ is the Uranian physical radius given by $r_{\rm U} \simeq 2.5 \times 10^7$ m, and $\Sigma_{\rm g,U0}$ is the initial disk surface density at $r = r_{\rm U}$.

In the original self-similar solution, $t_{\rm diff}$ (equation (13)) is a constant with time. However, in our case, $\nu \propto \Sigma_{\rm g}^{1/3}$. As the disk viscously expands and $\Sigma_{\rm g}$ decreases, ν at $r = r_{\rm d0}$ in equation (13) also decreases. As a result, $t_{\rm diff}$ increases. Because we are concerned with $t > t_{\rm diff}$, $t_* \propto t_{\rm diff}^{-1} \propto \nu \propto \Sigma_{\rm g}^{1/3}$. Taking this effect into account, equation (14) suggests $\Sigma_{\rm g} \propto t_{*0}^{-7/5}\Sigma_{\rm g}^{(-7/5)\times(1/3)}$, that is, $\Sigma_{\rm g} \propto t_{*0}^{-21/22}$, where $t_{*0} = 1 + t/t_{\rm diff0}$, and $t_{\rm diff0}$ is defined by quantities at $t = 0$ as (equation (13) with $\zeta = 3/4$):

$$t_{\rm diff0} = \frac{16}{75}\left(\frac{r^2}{\nu}\right)_{r_{\rm d0},t=0} \tag{15}$$

Because $\Sigma_{\rm g} \propto t_{*0}^{-21/22}$ and $t_* \propto t_{*0}\Sigma_{\rm g}^{1/3} \propto t_{*0}^{15/22}$, the final formula is:

$$\Sigma_{\rm g} = \Sigma_{\rm g,U0}\ t_{*0}^{-21/22}\left(\frac{r}{r_{\rm U}}\right)^{-3/4} \exp\left[-\left(\frac{r}{r_{\rm d0}}\right)^{5/4} t_{*0}^{-15/22}\right] \tag{16}$$

$$t_{*0} = 1 + t/t_{\rm diff0} \tag{17}$$

Although this formula is no longer a strict self-similar solution, it reproduces the numerical solution well, as shown in Fig. 2.

Initial relaxation to the self-similar solution. The impact-generated disk is quickly relaxed to the analytical quasi-steady-state self-similar solution (equation (16)). The parameters $r_{\rm d0}$ and $\Sigma_{\rm g,U0}$ in the self-similar solution are estimated by the total mass ($M_{\rm d,imp}$) and the angular momentum ($J_{\rm d,imp}$) of the impact-generated disk. In general, SPH simulations show that the impact-generated disk is compact and the mean radius is $\langle r_{\rm d,imp}\rangle \simeq 2r_{\rm U}$ (refs. [1,3,4]), where $\langle r_{\rm d,imp}\rangle$ is defined with the specific angular momentum, $j_{\rm d,imp} = J_{\rm d,imp}/M_{\rm d,imp}$, by $\langle r_{\rm d,imp}\rangle = \left(j_{\rm d,imp}/r_{\rm U}^2\Omega_{\rm U}\right)^2 r_{\rm U}$. The value of $\langle r_{\rm d,imp}\rangle$ is larger for a less steep disk surface density distribution. In the SPH impact simulations, debris particles generally have eccentric orbits. Since the orbits should be eventually circularized, conserving angular momentum, we define $\langle r_{\rm d,imp}\rangle$ with the assumption that the orbits are circular, while $j_{\rm d,imp}$ must be calculated from debris particles in eccentric orbits in the simulation results.

Because the radial gradient of the disk surface density is generally very steep, the disk expands to a self-similar distribution, almost maintaining the total disk angular momentum. While the total angular momentum is conserved, the innermost disk generally tends to spiral in by losing angular momentum. The one-dimensional diffusion simulations in this paper show that half of the mass inside $\langle r_{\rm d,imp}\rangle$ falls onto the planet until the disk settles down to the self-similar solution. If we consider the disk surface density distribution just after the impact as $\Sigma_{\rm g} \propto r^{-3}$ with a truncation at $r = 10r_{\rm U}$, as suggested by SPH simulations, the initial mass of the impact-generated disk ($M_{\rm d,imp}$) is decreased by about 20% in the early relaxation. Using $J_{\rm d,imp}$ of the impact-generated disk and the modified disk mass $0.8M_{\rm d,imp}$, we can evaluate $r_{\rm d0}$ and $\Sigma_{\rm g,U0}$ in the self-similar solution as follows.

The total disk mass and angular momentum of the self-similar solution are:

$$\begin{aligned} M_{\rm d,ss} &= \int_{r_{\rm U}}^{\infty} 2\pi r\Sigma_{\rm g}{\rm d}r = \tfrac{8\pi}{5} r_{\rm U}^2\Sigma_{\rm g,U0}\left(\tfrac{r_{\rm d0}}{r_{\rm U}}\right)^{5/4} {\rm e}^{-(r_{\rm d0}/r_{\rm U})^{-5/4}} \\ &\simeq \tfrac{8\pi}{5} r_{\rm U}^2\Sigma_{\rm g,U0}\left(\tfrac{r_{\rm d0}}{r_{\rm U}}\right)^{5/4} \times 0.776 \end{aligned} \tag{18}$$

$$\begin{aligned} J_{\rm d,ss} &= \int_{r_{\rm U}}^{\infty} 2\pi r\Sigma_{\rm g}\sqrt{GM_{\rm U}r}\ {\rm d}r = \tfrac{8\pi}{5} r_{\rm U}^4\Omega_{\rm U}\Sigma_{\rm g,U0}\left(\tfrac{r_{\rm d0}}{r_{\rm U}}\right)^{7/4} \Gamma\left(\tfrac{7}{5}, \left(\tfrac{r_{\rm d0}}{r_{\rm U}}\right)^{-5/4}\right) \\ &\simeq \tfrac{8\pi}{5} r_{\rm U}^4\Sigma_{\rm g,U0}\Omega_{\rm U}\left(\tfrac{r_{\rm d0}}{r_{\rm U}}\right)^{7/4} \times 0.797 \end{aligned} \tag{19}$$

where Γ is a 2nd-kind incomplete gamma function, $\Omega_{\rm U}$ is the disk orbital frequency at $r = r_{\rm U}$, and we used $r_{\rm d0}/r_{\rm U} \simeq 3$ to evaluate ${\rm e}^{-(r_{\rm d0}/r_{\rm U})^{-5/4}}$ and $\Gamma\left(\frac{7}{5}, (r_{\rm d0}/r_{\rm U})^{-5/4}\right)$. From equations (18) and (19), the mean specific angular momentum of the self-similar solution is given by:

$$j_{\rm d,ss} \simeq \frac{J_{\rm d,ss}}{M_{\rm d,ss}} = 1.03\left(\frac{r_{\rm d0}}{r_{\rm U}}\right)^{1/2}\Omega_{\rm U}r_{\rm U}^2 \tag{20}$$

Because $j_{\rm d,ss} = J_{\rm d,ss}/M_{\rm d,ss} \simeq J_{\rm d,imp}/0.8M_{\rm d,imp} \simeq 1.25\, j_{\rm d,imp}$:

$$r_{\rm d0} \simeq 1.47\left(\frac{j_{\rm d,imp}}{r_{\rm U}^2\Omega_{\rm U}}\right)^2 r_{\rm U} = 1.47\ \langle r_{\rm d,imp}\rangle \tag{21}$$

From equation (18) with $M_{\rm d,ss} \simeq 0.8\ M_{\rm d,imp}$, the surface density of the self-similar solution after the initial relaxation of the impact-generated disk is:

$$\begin{aligned} \Sigma_{\rm g,U0} &\simeq 0.256\left(\tfrac{r_{\rm d0}}{r_{\rm U}}\right)^{-5/4}\left(\tfrac{M_{\rm d,ss}}{r_{\rm U}^2}\right) \\ &\simeq 6.5\times 10^7\left(\tfrac{\langle r_{\rm d,imp}\rangle}{2r_{\rm U}}\right)^{-5/4}\left(\tfrac{M_{\rm d,imp}}{10^{-2}M_{\rm U}}\right)\ {\rm kg\ m^{-2}} \end{aligned} \tag{22}$$

In the case of the impact-generated disk with $\Sigma_{\rm g} = \Sigma_{\rm g,imp0}(r/r_{\rm U})^{-3}$ with a truncation at $r = 10r_{\rm U}$, $M_{\rm d,imp} = 0.9\times 2\pi\Sigma_{\rm g,imp0}\ r_{\rm U}^2$ and $\langle r_{\rm d,imp}\rangle \simeq 2.25\ r_{\rm U}$, so that $r_{\rm d0} \simeq 3.3\ r_{\rm U}$ and $\Sigma_{\rm g,U0} \simeq 0.26\Sigma_{\rm g,imp0}$.

As discussed in the main text, to evaluate the outer limit of the ice condensation, the envelope curve of the superposition of the $\Sigma_{\rm g}$–r curves at all the different times is important. The $\Sigma_{\rm g}$-distribution of the analytical solution starts exponentially declining at $r_{\rm d} \simeq r_{\rm d0}\ t_{*0}^{12/22}$ and the absolute values of $\Sigma_{\rm g}$ at the same r scale by $t_{*0}^{-21/22}$, while $\Sigma_{\rm g}$ further decreases in proportion to $r_{\rm d}^{-3/4} \propto t_{*0}^{-9/22}$, as shown in equation (16). Therefore, the envelope curve is given by:

$$\begin{aligned} \Sigma_{\rm g,env} &\simeq \Sigma_{\rm g,U0}\left(\tfrac{r}{r_{\rm U}}\right)^{-[(21+9)/22]/(12/22)} \\ &\simeq 6.5\times 10^7\left(\tfrac{\langle r_{\rm d,imp}\rangle}{2r_{\rm U}}\right)^{-5/4}\left(\tfrac{M_{\rm d,imp}}{10^{-2}M_{\rm U}}\right)\left(\tfrac{r}{r_{\rm U}}\right)^{-5/2}\ {\rm kg\,m^{-2}} \end{aligned} \tag{23}$$

It agrees with the numerical result in Fig. 2. The intersection radius between $\Sigma_{\rm g,env}$ and $\Sigma_{\rm g}$ at the ice condensation (equation (47)) is given by:

$$r_{\rm max} \simeq 20\left[\beta\left(\frac{\langle r_{\rm d,imp}\rangle}{2r_{\rm U}}\right)^{-5/4}\left(\frac{M_{\rm d,imp}}{10^{-2}M_{\rm U}}\right)\right]^{1/4} r_{\rm U} \tag{24}$$

Icy grain growth/drift and disk diffusion timescales. Here we show that the growth of condensed icy particles is much faster than their radial drift and the gas disk diffusion. Thereby, the condensed icy grains quickly grow in situ to kilometre-sized 'satellitesimals', which are the building blocks of satellites, in the H/He gas disk. We estimate the timescales of individual processes at $r \simeq 20r_{\rm U}$ because most of the icy grains condense there.

Disk diffusion timescale. We consider a disk with a characteristic radius of $r_{\rm d0}$ and a turbulent viscosity of $\alpha c_{\rm s}^2\Omega^{-1}$, where $c_{\rm s}$ is the local sound velocity of the disk gas, Ω is the local orbital frequency of the gas, and α is a parameter to represent the strength of turbulence ($\alpha \ll 1$)[13]. From equations (16) and (17), the disk diffusion timescale is given by:

$$t_{\rm diff} \simeq \frac{\Sigma_{\rm g}}{{\rm d}\Sigma_{\rm g}/{\rm d}t} \simeq t_{\rm diff0}\ t_{*0} \simeq \max(t_{\rm diff0}, t) \tag{25}$$

where $t_{\rm diff0}$ is the initial disk diffusion timescale given by:

$$t_{\rm diff0} \simeq \left(\frac{16r^2}{75\nu}\right)_{r_{\rm d0},t=0} \simeq \frac{16}{75\ \alpha}\left[\left(\frac{c_{\rm s}}{v_{\rm K}}\right)^{-2}\Omega^{-1}\right]_{r_{\rm d0},t=0} \tag{26}$$

The value of $c_{\rm s}/v_{\rm K}$, which is equivalent to the disk aspect ratio, is:

$$\frac{c_{\rm s}}{v_{\rm K}} \simeq 0.0564\left(\frac{T}{240\ {\rm K}}\right)^{1/2}\left(\frac{r}{r_{\rm U}}\right)^{1/2} \tag{27}$$

where we use a mean molecular weight of about 2.8. Substituting equations (6) and (7) into equation (27), for the initial self-similar disk after the relaxation:

$$\left(\frac{c_{\rm s}}{v_{\rm K}}\right)_{r_{\rm d0},t=0} \simeq 0.416\left(\frac{\langle r_{\rm d,imp}\rangle}{2r_{\rm U}}\right)^{-5/8}\left(\frac{M_{\rm d,imp}}{10^{-2}M_{\rm U}}\right)^{1/2}\left(\frac{r_{\rm d0}}{r_{\rm U}}\right)^{1/8} \tag{28}$$

Adopting a typical impact-generated disk with $\langle r_{\rm d,imp}\rangle \simeq 2\ r_{\rm U}$ and $M_{\rm d,imp} \simeq 10^{-2}M_{\rm U}$ and the corresponding relaxed disk with $r_{\rm d0} \simeq 3\ r_{\rm U}$, and scaling Ω^{-1} at $r \simeq 20r_{\rm U}$, equation (26) reads as follows:

$$t_{\rm diff0} \simeq 54\left(\frac{\alpha}{10^{-3}}\right)^{-1}\Omega^{-1} \tag{29}$$

Because $\Sigma_g \propto t_{*0}^{-21/22}$, the time from the initial Σ_g given by equation (6) to Σ_g at the ice condensation given by equation (8) at $r \simeq 20$ astronomical units is:

$$\begin{aligned} t &\simeq t_{*0}\ t_{\rm diff0} \simeq \left(\frac{\Sigma_{g,\{\rm equation(6)\}}}{\Sigma_{g,\rm equation(8)}}\right)^{22/21} t_{\rm diff0} \\ &\simeq 1.7\times10^4\left[\beta\left(\frac{\langle r_{\rm d,imp}\rangle}{2r_U}\right)^{-5/4}\left(\frac{M_{\rm d,imp}}{10^{-2}M_U}\right)\right]^{22/21} t_{\rm diff0} \end{aligned} \tag{30}$$

Therefore, the disk diffusion timescale at the ice condensation is:

$$\begin{aligned} t_{\rm diff} &\simeq t \simeq 9.2\times10^5 \\ &\times\left[\beta\left(\frac{\langle r_{\rm d,imp}\rangle}{2r_U}\right)^{-5/4}\left(\frac{M_{\rm d,imp}}{10^{-2}M_U}\right)\right]^{22/21}\left(\frac{\alpha}{10^{-3}}\right)^{-1}\Omega^{-1} \end{aligned} \tag{31}$$

Drift timescale of icy particles due to gas drag. The condensed icy grains coagulate with each other. As the icy particles grow, their motions become less coupled to the disk gas. The degree of the decoupling is represented by the Stokes number, $\mathrm{St} = t_{\rm stop}\Omega$, where $t_{\rm stop}$ is the stopping time due to the aerodynamic gas drag. The disk gas rotates more slowly than the particles by a small fraction of $\eta \simeq (c_s/v_K)^2 (\ll 1)$. As a result of the drag from the slower-rotating disk gas, the particles drift inward with the drift timescale given by[15]:

$$t_{\rm drift} \simeq \frac{r}{v_r} \simeq \frac{r}{2\eta\ v_K}\frac{1+\mathrm{St}^2}{\mathrm{St}} \simeq 0.5\left(\frac{c_s}{v_K}\right)^{-2}\frac{1+\mathrm{St}^2}{\mathrm{St}}\Omega^{-1} \tag{32}$$

where v_r is the radial drift velocity. At $r \simeq 20\ r_U$, $(c_s/v_K)^{-2} \simeq 16$ (equation (27)). The drift is the fastest at $\mathrm{St} \simeq 1$.

Growth timescale of icy particles. The growth timescale (the mass-doubling timescale) of icy particles with $\mathrm{St} \lesssim 1$ is given by:

$$t_{\rm grow} \simeq \frac{1}{n\pi R^2 \Delta v} \tag{33}$$

where R is the particle physical radius, n is their spatial number density:

$$n = \frac{\rho_p}{(4\pi/3)\rho_{\rm mat}R^3} \tag{34}$$

where ρ_p and $\rho_{\rm mat}$ are the spatial and material densities of the particles, and Δv is the relative velocity between the particles[22]:

$$\Delta v \simeq (3\alpha\mathrm{St})^{1/2} c_s \tag{35}$$

The icy particle spatial density is given by their surface density $\Sigma_{\rm ice}$ as[23]:

$$\rho_p \simeq \frac{\Sigma_{\rm ice}}{\sqrt{2\pi}h_p} \simeq \frac{\Sigma_{\rm ice}}{\sqrt{2\pi}h_g}\left(1+\frac{\mathrm{St}}{\alpha}\right)^{1/2} \tag{36}$$

where h_p and h_g are the particle and the gas vertical scale heights. Substituting equations (34), (35) and (36) into equation (33), we obtain:

$$t_{\rm grow} \simeq \frac{4\sqrt{2\pi}}{3\sqrt{3}}\frac{\rho_{\rm mat}R}{\sqrt{\mathrm{St}(\mathrm{St}+\alpha)}\ \Sigma_{\rm ice}}\Omega^{-1} \tag{37}$$

where we used the disk gas scale height as given by $h_g \simeq c_s\Omega^{-1}$.

In the situation we are considering, the drag law is mostly in the Stokes drag regime. In this case, the Stokes number is given by:

$$\mathrm{St} \simeq \frac{4\rho_{\rm mat}\sigma_{\rm coll}R^2\Omega}{9\mu_{\rm HHe}\ m_H\ c_s} \simeq 1.5\times10^{-6}\left(\frac{T_{\rm ice}}{240\ \mathrm{K}}\right)^{-1/2}\left(\frac{R}{\mu\mathrm{m}}\right)^2\left(\frac{r}{r_U}\right)^{-3/2} \tag{38}$$

where we used $\rho_{\rm mat} \simeq 10^3\ \mathrm{kg/m^3}$, $\mu_{\rm HHe} \simeq 2.4$ is the mean molecular weight for H-He gas, $m_H \simeq 1.67\times10^{-21}$ kg is the hydrogen mass, and $\sigma_{\rm col} \simeq 2\times10^{-11}\ \mathrm{m^2}$ is the collision cross-section. Substituting equations (50) and (8) into equation (37), we obtain:

$$t_{\rm grow} \simeq 1\left(\frac{\mathrm{St}+\alpha}{10^{-4}}\right)^{-1/2}\left(\frac{\gamma}{0.3}\right)^{-1}\left(\frac{\alpha}{10^{-3}}\right)\left(\frac{T_{\rm ice}}{240\ \mathrm{K}}\right)^{-11/4}\left(\frac{r}{r_U}\right)^{-3/4}\Omega^{-1} \tag{39}$$

Timescale comparison. Because $c_s < v_K$ and $\alpha \ll 1$:

$$t_{\rm grow} \ll t_{\rm drift}, t_{\rm diff} \tag{40}$$

Around $\mathrm{St} \simeq 1$:

$$t_{\rm grow} \ll t_{\rm drift} \ll t_{\rm diff}. \tag{41}$$

These results imply that the condensed icy grains quickly grow to kilometre-sized satellitesimals in situ in the H/He gas disk. The satellitesimal motions are decoupled from the disk gas.

Ice condensation. Icy grains condense when the vapour pressure exceeds the vapour saturation pressure. Because the vapour saturation pressure depends sensitively on temperature, the condensation condition is often described by $T < T_{\rm ice}$, where $T_{\rm ice}$ is the condensation temperature given by[24]:

$$T_{\rm ice} \simeq \frac{A}{B - \log_{10}[P_{\rm H2O}\ (\mathrm{Pa})]}\ \mathrm{K} \tag{42}$$

with:

$$A \simeq 2633\ ;\ B \simeq 12.06 \tag{43}$$

where $P_{\rm H2O}$ is the partial pressure of water vapour in the disk, given by:

$$P_{\rm H2O} = \gamma\ \frac{\mu_{\rm all}}{\mu_{\rm H2O}}P \simeq 0.156\ \gamma\ P \tag{44}$$

where P is the total pressure, $\gamma = \Sigma_{\rm H2O}/\Sigma_g$, and $\mu_{\rm all} \simeq 2.8$ and $\mu_{\rm H2O} = 18$ are the total and H_2O mean molecular weight.

The total pressure is:

$$P = \rho_g c_s^2 = \frac{\Sigma_g}{\sqrt{2\pi}}c_s\Omega \simeq 61.9\left(\frac{\alpha}{10^{-3}}\right)^{-1}\left(\frac{T}{240\ \mathrm{K}}\right)^{7/2}\ \mathrm{Pa} \tag{45}$$

where we used:

$$c_s \simeq 8.41\times10^2\ (\mu_{\rm all}/2.8)^{-1/2}(T/240\ \mathrm{K})^{1/2}\ \mathrm{m\,s^{-1}} \tag{46}$$

and Σ_g obtained by equation (2) is:

$$\Sigma_g \simeq 4.02\times10^2\left(\frac{\alpha}{10^{-3}}\right)^{-1}\left(\frac{T}{240\ \mathrm{K}}\right)^3\left(\frac{r}{r_U}\right)^{3/2}\ \mathrm{kg\,m^{-2}} \tag{47}$$

Thereby:

$$P_{\rm H2O} = 0.156\ \gamma P \simeq 9.66\gamma\left(\frac{\alpha}{10^{-3}}\right)^{-1}\left(\frac{T}{240\ \mathrm{K}}\right)^{7/2}\ \mathrm{Pa} \tag{48}$$

From equations (42) and (48) with $T = T_{\rm ice}$, we found:

$$\begin{aligned} T_{\rm ice} &\simeq \frac{2633}{12.06-0.98-\log_{10}\left[\frac{\gamma}{0.3}\left(\frac{\alpha}{10^{-3}}\right)^{-1}\right]}\ \mathrm{K} \\ &\simeq \frac{238}{1-\frac{1}{11.08}\log_{10}\left[\frac{\gamma}{0.3}\left(\frac{\alpha}{10^{-3}}\right)^{-1}\right]}\ \mathrm{K} \simeq 238 + 21\ \log_{10}\left[\frac{\gamma}{0.3}\left(\frac{\alpha}{10^{-3}}\right)^{-1}\right]\ \mathrm{K} \end{aligned} \tag{49}$$

Note that the r-dependence vanishes for $T_{\rm ice}$ in our disk model.

Barriers for silicate particle sticking. When collision velocity exceeds a threshold value (about 1 $\mathrm{m\,s^{-1}}$), silicate–silicate collisional sticking is inhibited by rebounding or fragmentation[17]. In the parameter range we consider, the particle collision velocity induced by turbulence is given by equations (35) and (46). The maximum Stokes number of the particles that allows the sticking is given by $v_{\rm bf} \simeq \Delta v$ as:

$$\begin{aligned} \mathrm{St}_{\rm max} &\simeq \frac{1}{3\alpha}\left(\frac{v_{\rm bf}}{c_s}\right)^2 \\ &\simeq 5\times10^{-4}\left(\frac{\alpha}{10^{-3}}\right)^{-1}\left(\frac{v_{\rm bf}}{1\mathrm{m\,s^{-1}}}\right)^2\left(\frac{\mu_{\rm all}}{2.8}\right)\left(\frac{T}{240\ \mathrm{K}}\right)^{-1} \end{aligned} \tag{50}$$

Thus, silicates can grow only up to $\mathrm{St} \simeq 5\times10^{-4}$ until T deceases to the ice condensation temperature of about 240 K. In the Stokes drag regime, it corresponds to a particle size of around 100 μm. The silicate particles can form satellitesimals only after ices condense and they stick to the icy particles or ices condense to their surface.

N-body simulation. We perform a three-dimensional N-body simulation from 10,000 bodies (satellitesimals) with individual masses $0.92\times10^{-8}\ M_U$ with the predicted ice distribution given by equation (8) with $r_{\rm max} = 20r_U$ and $\beta = \gamma_{03} = 1$. Gravitational interactions of all the bodies are included. Aerodynamical gas drag to satellitesimals and type I migration due to disk–planet interactions are neglected as below. Tidal interactions with Uranus are also neglected, because the timescale of our run is too short for the effect to be important. We assume perfect accretion and the physical radii are increased by a factor of 2 to accelerate the growth. Small eccentricities and inclinations are given initially. They are quickly relaxed by gravitational stirring and collision damping. We note that since there is no large reservoir of icy particles in the outer region of the disk and no icy particle supply from outside the Uranian system, pebble accretion is not effective and satellitesimals grow through mutual collisions.

When a proto-satellite grows, type I migration due to the torque from the density waves in the gas disk can become important. However, we show that its timescale is longer than the disk diffusion timescale and its effect is negligible. The migration timescale of a satellite with mass m is[25]:

$$t_{\rm mig} \simeq \frac{1}{2.7+1.1\times(3/4)}\left(\frac{M_U}{m}\right)\left(\frac{M_U}{\Sigma_g r^2}\right)\left(\frac{c_s}{v_K}\right)^2\Omega^{-1} \tag{51}$$

Because type I migration is caused by a residual between the inner and outer disk torques and between the Lindblad and corotation torques, the numerical factor depends on the gas disk structure (sometimes it changes the sign). However, the absolute value of the timescale is generally of the same order for any disk structure. At the ice condensation with $T \simeq 240$ K at $r \simeq 20 r_{\rm U}$, $c_{\rm s}/v_{\rm K} \simeq 0.25$ (equation (27)). For $m/M_{\rm U} \simeq 3 \times 10^{-5}$ and $\Sigma_{\rm g} r^2/M_{\rm U} \simeq 10^{-4}$, where we consider the most-massive satellites, the type I migration timescale is $t_{\rm mig} \simeq 0.6 \times 10^7\, \Omega^{-1}$. Because $t_{\rm diff}$ at the ice condensation is approximately $0.9 \times 10^6 \Omega^{-1}$ (equation (29)) and the H/He gas should decay more when the large enough satellites grow from satellitesimals, it is predicted that $t_{\rm mig} \gg t_{\rm diff}$. Because $t_{\rm diff} \propto t_{*0} \propto \Sigma_{\rm g}^{-22/21}$ and $t_{\rm mig} \propto 1/\Sigma_{\rm g}$, the relation of $t_{\rm mig} \gg t_{\rm diff}$ does not change afterwards. Therefore, type I migration of proto-satellites is negligible.

Isolation mass in oligarchic growth. In the context of planet accretion, if orbital migration is neglected, the planetary accretion is terminated when small bodies in the feeding zone of the planet are consumed, and the planetary mass at that point is called 'isolation mass.'[18] In the system we consider here, the isolation mass ($m_{\rm iso}$) is defined by:

$$m_{\rm iso} = 2\pi r \Delta r \Sigma_{\rm ice} \tag{52}$$

where Δr is the orbital distance between proto-satellites and $\Delta r \simeq 10(2m_{\rm iso}/3M_{\rm U})^{1/3} r$. It is rewritten as:

$$\begin{aligned} \frac{m_{\rm iso}}{M_{\rm U}} &\simeq \frac{10 \times 2^{1/3}}{3^{1/3}} \left(\frac{2\pi \Sigma_{\rm ice} r^2}{M_{\rm U}} \right)^{3/2} \\ &\simeq 0.74 \times 10^{-4} \beta^{-3/2} \gamma_{03}^{3/2} \left(\frac{r}{20 r_{\rm U}} \right)^{21/4} \end{aligned} \tag{53}$$

The steep radial gradient of $m_{\rm iso}$ explains the orbital configuration of the current Uranian satellites (Fig. 1).

Data availability

The data that support the plots within this paper and other findings of this study are available from the corresponding author upon reasonable request.

Code availability

The codes used in this study are available from the corresponding author upon reasonable request.

Received: 27 July 2019; Accepted: 14 February 2020;
Published online: 30 March 2020

References

1. Slattery, W. L., Benz, W. & Cameron, A. G. W. Giant impacts on a primitive Uranus. *Icarus* **99**, 167–174 (1992).
2. Kurosaki, K. & Inutsuka, S.-i The exchange of mass and angular momentum in the impact event of ice giant planets: implications for the origin of Uranus. *Astron. J.* **157**, 13 (2019).
3. Reinhardt, C., Chau, A., Stadel, J. & Helled, R. Bifurcation in the history of Uranus and Neptune: the role of giant impacts. *Mon. Not. R. Astron. Soc.* **492**, 5336–5353 (2020).
4. Kegerreis, J. A. et al. Consequences of giant impacts on early Uranus for rotation, internal structure, debris, and atmospheric erosion. *Astrophys. J.* **861**, 52 (2018).
5. Canup, R. M. & Asphaug, E. Origin of the Moon in a giant impact near the end of the Earth's formation. *Nature* **412**, 708–712 (2001).
6. Ida, S., Canup, R. M. & Stewart, G. R. Lunar accretion from an impact-generated disk. *Nature* **389**, 353–357 (1997).
7. Dermott, S. F., Malhotra, R. & Murray, C. D. Dynamics of the Uranian and Saturnian satellite systems: a chaotic route to melting Miranda? *Icarus* **76**, 295–334 (1988).
8. Hussmann, H., Sohl, F. & Spohn, T. Subsurface oceans and deep interiors of medium-sized outer planet satellites and large trans-Neptunian objects. *Icarus* **185**, 258–273 (2006).
9. Podolak, M., Weizman, A. & Marley, M. Comparative models of Uranus and Neptune. *Planet. Space Sci.* **43**, 1517–1522 (1995).
10. Szulágyi, J., Cilibrasi, M. & Mayer, L. In situ formation of icy moons of Uranus and Neptune. *Astrophys. J.* **868**, L13 (2018).
11. Morbidelli, A., Tsiganis, K., Batygin, K., Crida, A. & Gomes, R. Explaining why the Uranian satellites have equatorial prograde orbits despite the large planetary obliquity. *Icarus* **219**, 737–740 (2012).
12. Hartmann, L., Calvet, N., Gullbring, E. & D'Alessio, P. Accretion and the evolution of T Tauri disks. *Astrophys. J.* **495**, 385–400 (1998).
13. Shakura, N. I. & Sunyaev, R. A. Black holes in binary systems. Observational appearance. *Astron. Astrophys.* **500**, 33–51 (1973).
14. Lynden-Bell, D. & Pringle, J. E. The evolution of viscous discs and the origin of the nebular variables. *Mon. Not. R. Astron. Soc.* **168**, 603–637 (1974).
15. Nakagawa, Y., Sekiya, M. & Hayashi, C. Settling and growth of dust particles in a laminar phase of a low-mass solar nebula. *Icarus* **67**, 375–390 (1986).
16. Melosh, H. J. A hydrocode equation of state for SiO_2. *Meteorit. Planet. Sci.* **42**, 2079–2098 (2007).
17. Blum, J. & Wurm, G. Experiments on sticking, restructuring, and fragmentation of preplanetary dust aggregates. *Icarus* **143**, 138–146 (2000).
18. Kokubo, E. & Ida, S. Formation of protoplanets from planetesimals in the solar nebula. *Icarus* **143**, 15–27 (2000).
19. Ishizawa, Y., Sasaki, T. & Hosono, N. Can the Uranian satellites form from a debris disk generated by a giant impact? *Astrophys. J.* **885**, 132 (2019).
20. Agnor, C. B. & Hamilton, D. P. Neptune's capture of its moon Triton in a binary-planet gravitational encounter. *Nature* **441**, 192–194 (2006).
21. Rogers, L. A. Most 1.6 Earth-radius planets are not rocky. *Astrophys. J.* **801**, 41 (2015).
22. Ormel, C. W. & Cuzzi, J. N. Closed-form expressions for particle relative velocities induced by turbulence. *Astron. Astrophys.* **466**, 413–420 (2007).
23. Dubrulle, B., Morfill, G. & Sterzik, M. The dust subdisk in the protoplanetary nebula. *Icarus* **114**, 237–246 (1995).
24. Lichtenegger, H. I. M. & Komle, N. I. Heating and evaporation of icy particles in the vicinity of comets. *Icarus* **90**, 319–325 (1991).
25. Tanaka, H., Takeuchi, T. & Ward, W. R. Three-dimensional interaction between a planet and an isothermal gaseous disk. I. Corotation and Lindblad torques and planet migration. *Astrophys. J.* **565**, 1257–1274 (2002).

Acknowledgements

This study was supported by MEXT 'Exploratory Challenge on Post-K computer' (hp180183 and hp190143), by 'Priority Issue on post-K computer' (hp190156), by JSPS KAKENHI 15H02065 and 19K03950, and by MEXT KAKENHI 18H05438. The *N*-body simulation in this work was carried out at the Yukawa Institute Computer Facility.

Author contributions

S.I, S.U. and T.S. initiated the project. S.I. and Y.I. performed the theoretical calculations. S.I. wrote the manuscript. All authors contributed to the discussion and the interpretation of the results.

Competing interests

The authors declare no competing interests.

Additional information

Correspondence and requests for materials should be addressed to S.I.

Reprints and permissions information is available at www.nature.com/reprints.

Publisher's note Springer Nature remains neutral with regard to jurisdictional claims in published maps and institutional affiliations.